Measurement 248 (2025) 116889

Contents lists available at ScienceDirect

Measurement

journal homepage: www.elsevier.com/locate/measurement

Monitoring ZnO surge arresters using convolutional neural networks and image processing techniques combined with signal alignment

Bruno Vinicius Silveira Araujo [a,d], Gustavo Aragão Rodrigues [a,d], Johnny Herbert Paixão de Oliveira [a,d], George Victor Rocha Xavier [a,d], Ulisses Daniel Enes de Souza Lebre [b], Charles Antony Cordeiro de Araujo [b], Eduardo Oliveira Freire [a,d], Estácio Tavares Wanderley Neto [c], Tarso Vilela Ferreira [a,d,*]

[a] Federal University of Sergipe, Brazil
[b] ENEVA S.A, Brazil
[c] Federal University of Itajubá, Brazil
[d] INESC P&D Brasil, Brazil

ARTICLE INFO

Keywords:
Automatic diagnosis
Computer vision
Electrical equipment
High voltage
Neural network
Thermography

ABSTRACT

Monitoring and preemptive maintenance of high-voltage electrical equipment play a crucial role in preventing breakdowns and ensuring the seamless operation of power systems. Infrared monitoring stands out due to its convenience, safety protocols, and utilization of temperature as a key indicator for assessing the structural integrity and component health of equipment. This paper introduces a method for monitoring ZnO lightning arresters by analyzing their thermal profiles. The approach involves employing a convolutional neural network and computer vision processes to detect, segment, and extract thermal data from these devices. An alignment algorithm facilitates comparison and classification of operational integrity. The method provides an accurate and comprehensive evaluation of ZnO lightning arresters, enabling continuous monitoring and efficient diagnosis. By analyzing thermal imaging data from a 500 kV substation and conducting laboratory tests on both healthy and intentionally defective equipment, the detection algorithm achieves favorable precision rates (0.861), recall (0.855), mAP50 (0.903), and mAP50:95 (0.615), ensuring precise detection and segmentation. Despite variations caused by thermal imager measurement errors, distance fluctuations, angle deviations, and environmental factors, the algorithm consistently identifies both normally operating and faulty equipment. Notably, when assessing healthy and intentionally defective equipment, the method achieves excellent accuracy in anomalies and its locations.

1. Introduction

In modern society, there is increasing demand for higher levels of reliability, continuity in power supply, and quality of electrical power systems (EPSs). It is crucial that the equipment comprising a EPS remains consistently operable, as failures can result in interruptions to the power supply or compromised quality [1].

The components of an EPS include transformers, insulators, potential transformers (PTs), current transformers (CTs), disconnect switches, circuit breakers, and surge arresters (SAs). SAs serve as voltage limiters, preventing values above a pre-defined threshold, and are standardized to provide a margin of safety for the equipment they are safeguarding [2].

Under normal, steady-state conditions, a small leakage current flows through an SA due to the semiconductor nature of the varistors, which are typically made from zinc oxide (ZnO). This current generates heat within the SA through the Joule effect, although at a controlled rate that prevents an excessive temperature rise [3]. These devices are also

* Corresponding author.
E-mail addresses: bruno.silveira@inescbrasil.org.br (B.V. Silveira Araujo), gustavo.rodrigues@inescbrasil.org.br (G.A. Rodrigues), john3008@academico.ufs.br (J.H. Paixão de Oliveira), george.xavier@academico.ufs.br (G.V. Rocha Xavier), ulisses.lebre@eneva.com.br (U.D.E.S. Lebre), charles.cordeiro@eneva.com.br (C.A.C. de Araujo), efreire@academico.ufs.br (E.O. Freire), estacio@lat-efei.org.br (E.T. Wanderley Neto), tarso@academico.ufs.br (T.V. Ferreira).

https://doi.org/10.1016/j.measurement.2025.116889
Received 11 April 2024; Received in revised form 14 January 2025; Accepted 28 January 2025
Available online 30 January 2025

exposed to adverse environmental conditions, such as saline pollution, as well as unpredictable events such as lightning strikes and switching surges, which can potentially damage them.

Hence, monitoring these devices and conducting preventive maintenance are crucial in order to anticipate potential failures and ensure full operation and reliability of the EPS. Among the various monitoring techniques available for high-voltage equipment, the most notable include leakage current measurement, ultraviolet monitoring, and infrared monitoring. Infrared monitoring stands out due to its practicality and safety, and particularly because the temperature of the equipment is one of the most important indicators of its condition [4].

In view of these factors and the significance that infrared monitoring has acquired over the years, various studies have been carried out with the aim of analyzing and processing infrared images of high-voltage electrical equipment and its components. There are several areas of research related to infrared imaging, and some of these studies have focused on preprocessing and enhancing the quality of thermal images [5–7], which can facilitate the segmentation and detection of equipment and its components.

Current research on the diagnosis of faults in high-voltage electrical equipment using infrared imaging focuses on detecting and/or segmenting regions of interest, depending on the equipment being assessed, using a range of techniques documented in the relevant literature [8–16]. Feature extraction techniques can be applied to these regions of interest to detect and/or classify equipment faults, using various procedures, as described in [17–30].

Among existing studies related to detecting and segmenting regions of interest in electrical equipment using thermal images, several approaches stand out, for example those based on artificial neural networks (ANNs), deep learning algorithms, and convolutional neural networks (CNNs) such as YOLO (You Only Look Once) [9–13]. Researchers have also assessed the performance of different detection and segmentation algorithms such as Faster R-CNN, YOLOv3, Otsu, and fuzzy C-means [14–16].

With regard to the attribute extraction and/or fault classification stages, the authors of [17–19] developed equations to assist in diagnosing and classifying thermal anomalies in electrical equipment. Li et al. [20] proposed a diagnostic method for suspension insulators of 500 kV and 220 kV power lines, and applied wavelet analysis to evaluate the standard deviation and the absolute maximum value of the gradient of the low-frequency temperature component along the axis of the polymeric core.

In addition to the studies mentioned above, several others have focused on the use of deep learning algorithms to optimize and enhance the accuracy and speed of processing thermal images, as well as the diagnosis of high-voltage electrical equipment [21–24,26–28]. For example, Ullah et al. [21] and Wang et al. [22] presented methods for classifying high-voltage electrical equipment (faulty and non-faulty) by training algorithms such as random forest (RF) and support vector machine (SVM) using features extracted from thermal images through CNNs. In 2021, Su et al. [23] and Lu et al. [24] introduced fault recognition methods based on the fusion of visible and infrared images of electrical equipment, coupled with CNN algorithms.

In order to optimize the visual inspection process, digital image processing, computer vision, and machine learning have been employed to extract thermal information and to achieve faster and more accurate fault diagnosis. Nevertheless, the identification, segmentation, and feature extraction of the thermal characteristics in the region of interest of infrared images with a complex background remain challenging, and many studies have therefore aimed to detect the region in which thermal anomalies (specifically heating) occur and to extract temperature values for diagnostic purposes [26–29]. However, by focusing exclusively on hotspots or areas with anomalies, other emerging defects in different parts of the equipment that do not yet manifest as hot or cold spots may be overlooked. Our analysis of the equipment's thermal profile enables not only the detection of hotspots and other thermal anomalies, but also the automatic localization of the anomaly. Furthermore, this analysis allows for the anticipation of regions that may become thermally anomalous in the future, providing a more comprehensive and predictive view of the equipment's condition.

The present article is aligned with the studies mentioned above, and proposes an automatic fault diagnosis method for electrical equipment with a focus on SAs. Our method utilizes a CNN and computer vision processes. For this purpose, thermal profiles of SAs, and more specifically the insulating column, were collected at different angles and times from the Porto de Sergipe I Thermoelectric Power Plant substation. In addition, thermographic images of healthy and faulty SAs from the work of Wanderley Neto et al. [3] were used. The dynamic time warping (DTW) algorithm was applied to align the thermal profile of the analyzed equipment with similar reference equipment and to assess the profile similarities. This approach was used together with qualitative rules based on those in [18] to classify the different operational conditions of the equipment, with the aim of determining its integrity, the type of anomaly (hot spot or cold spot), and its location.

This article is structured as follows: in Section 2, the methodology adopted for the construction and development of the study is described; in Section 3, the results obtained are analyzed and discussed; and in Section 4, some final considerations are presented.

2. Methodology

This study presents an innovative method for the automatic diagnosis of faults in SAs in which a CNN, YOLOv5, and image processing are used to identify, segment, and extract the thermal profile of both the analyzed equipment and the reference equipment.

An optimal alignment technique based on dynamic time warping (DTW) is also adopted to ensure that the thermal profiles of similar equipment, one healthy (reference) and the other under test (analyzed), are compared accurately. These methods are used together to classify the integrity of the equipment, identify the type of anomaly (hot or cold spot), and determine its location.

The proposed methodology comprises the following steps:

i. Database composition;
ii. Temperature matrix extraction;
iii. Processing of the temperature matrix and thermal image;
iv. Alignment of the thermal profiles;
v. Equipment diagnosis.

The aim of the proposed method is to provide a precise and reliable analysis of the integrity of an SA, in order to enable the early detection of potential faults and significantly enhance the efficiency of preventive maintenance procedures, thereby improving the overall safety and efficiency of the electrical system. In the following section, we give details of each of the methodological steps.

2.1. Database composition

Initially, a database of thermal images of high-voltage equipment was created, including transformers, PTs, CTs, disconnect switches, insulating columns, suspension insulators, and SAs. This database was used to train and validate the CNN used in the equipment detection process.

In this initial dataset, thermal images were exclusively captured from various angles, distances, times of day, dates, and weather conditions, totaling 2,839 images. Of these, approximately 30 % (852 images) were allocated for the model validation process (YOLOv5), while the remaining 1,987 images (70 %) were used for training. Fig. 1 shows thermographs captured from the high-voltage equipment.

Additionally, the training dataset, consisting of 1,987 images, was artificially expanded by creating grayscale versions of each of the original images, resulting in a total of 3,974 images in the training set.

Fig. 1. Thermographs of high-voltage equipment: (a) pedestal insulator; (b) surge arrester; (c) circuit breaker.

This increase ensures a more realistic and accurate assessment of the CNN's performance, guaranteeing that the model has a greater generalization capability, making it more reliable when dealing with real and unknown data. Therefore, a total of 4,642 images were used in the CNN training and validation process.

The conversion of thermal images to grayscale was chosen due to the variation in color palettes between different captures of the same equipment. By standardizing the color palette through grayscale conversion, the method proposed in this study ensures greater consistency in processing and analysis.

A second database was created for the application of the proposed method, consisting of 200 images of healthy ZnO SA in all three phases (A, B, and C). The capture angles and distances of these thermographs were pre-defined to match the images of different phases for the same equipment. Finally, the ambient temperature at the moment of thermograph capture was recorded.

To create both databases, we used a FLIR T840 thermal camera with a measurement range of −20 °C to 120 °C (−4°F to 248°F) and a reading accuracy of ± 2°C ± 2 %, with a 42° lens and a field of view of 42°×32°. Prior to thermography, the reflected temperature was determined based on the camera manual [30], and an emissivity of 0.92 was adopted, which is an approximate value for the material comprising the insulating columns (the object of analysis) with RTV coating. Thermographs were acquired at the substation of Porto de Sergipe I Thermoelectric Power Plant, owned by ENEVA S.A. Ambient temperature measurements were carried out at an air quality and meteorology monitoring station located 1.6 km from the substation, which was equipped with a RIKA temperature sensor.

To take into account the inherent measurement error of the thermal camera, we considered variations in distance (5 to 6 m), and the consequent subtle variations in angle, as well as the effect of environmental variables such as irradiation and shading on the extracted thermal profile. Eight thermal images of the same equipment were captured at 10:30 am on the same day.

In addition to evaluating the same equipment, a study was also conducted of equipment in different phases. Thermographs of SAs in phases A, B, and C were taken on different days and times (10 am, 11 am, 4 pm, 5 pm, 6 pm, and 7 pm) and at various angles (0°, 45°, 360°) in order to broaden the analysis and provide a more comprehensive view of the performance of our method under different conditions closely resembling a practical field application of the method. This is because a unit of equipment suspected of being defective can be compared with another unit of the same type, or with its historical thermal profiles, subject to similar conditions and normal operation.

Finally, to evaluate the proposed method on faulty SAs, we employed the database used in [3], which consists of 409 images. In this study, thermographs of a ZnO SA were acquired under normal operating conditions and after the intentional introduction of defects. Nine types of defect were introduced: internal short-circuits of a single varistor; short-circuits in a set of varistors; short-circuits in separate varistors; short-circuits in subsequent sets of varistors; broken varistors; loss of sealing; internal humidity; misalignment of the active column; and surface pollution. The tests were conducted at the High Voltage Laboratory of the Federal University of Campina Grande.

2.2. Extraction of the temperature matrix

To extract the temperature matrix (M_{temp}), we developed computational routines that made use of the Software Development Kit (SDK) provided by the thermal camera manufacturer (FLIR). This approach was preferred over curve fitting to relate the grayscale level of the image to the temperature of the equipment using the display temperature range, and has been employed in prior studies [25,26,29]. The choice to use the SDK was made due to the inevitability of losing temperature information from hot areas when they exceed the maximum level of the available color palette [27].

The libraries in this SDK were used to create a Python computational routine linking the pixels of the infrared image to the temperature detected by the thermal camera. Each resulting infrared image gave a temperature matrix with dimensions proportional to that of the thermal image.

2.3. Processing of the temperature matrix and thermal image

A flowchart for the processing of the temperature matrix and thermal images is presented in Fig. 2.

In the initial step, the region of interest of the monitored electrical equipment was detected using the open-source YOLOv5 CNN, which is appropriate for training and application. As described by Redmon et al. [31,32], YOLO addresses detection as a regression problem in which spatially separated bounding boxes and associated class probabilities are defined. Additionally, this CNN offers a good balance between processing time and detection accuracy, being widely used in various studies related to the detection of electrical equipment through thermal images [9,10,13,14].

For the training, a single label corresponding to the insulating column (region of interest) of the equipment in the substation was used. All insulating columns of the 500 kV substation equipment were included, with the aim of making the proposed method generalizable to any type of equipment. The labeling of the objects of interest was performed using the MakeSense platform. Additionally, YOLO was trained using pre-trained weights from the Microsoft COCO (Common Objects in Context) dataset, which contributed to the effectiveness of the training.

Training and validation of the database were carried out on a workstation with the following specifications: Windows 11 Pro 64-bit; two Intel® Xeon® Gold 6226R processors; 128 GB of RAM; Nvidia T1000 4 GB graphics card.

In the detection process, a file is generated that contains the labels

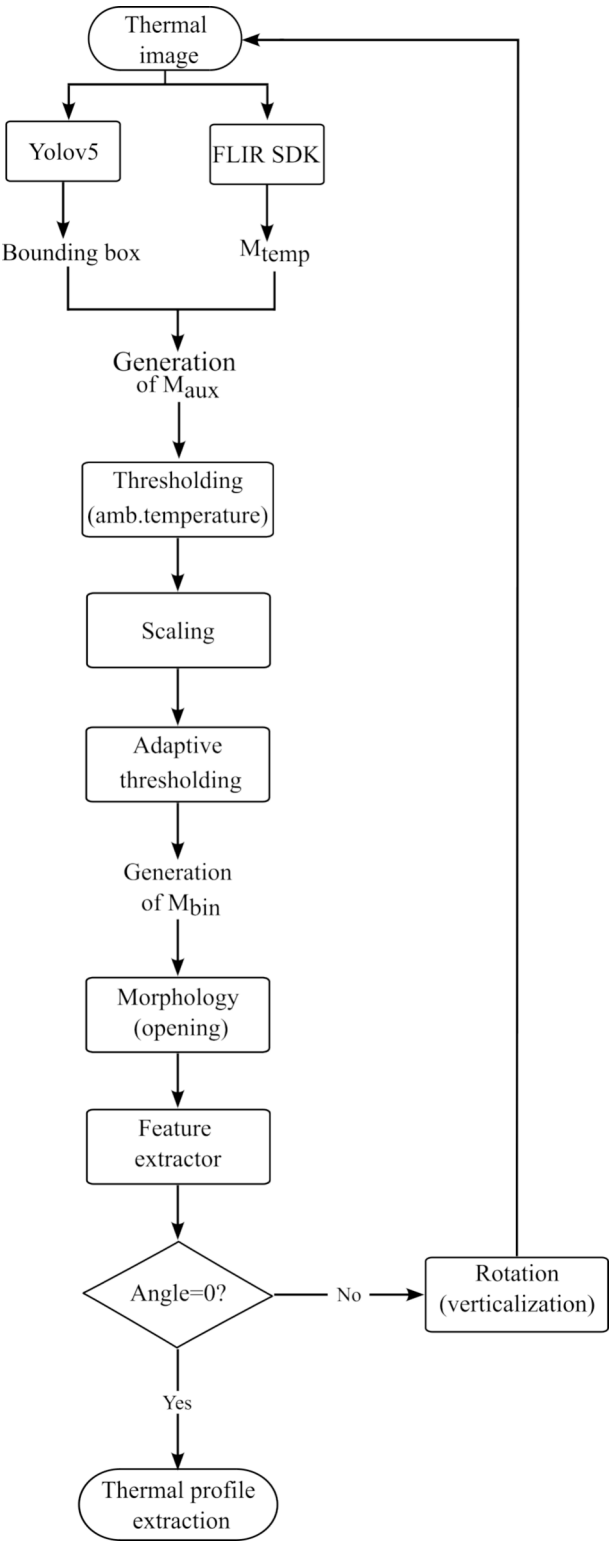

Fig. 2. Flowchart for processing of the temperature matrix and thermal image.

and coordinates of the bounding boxes encompassing the detected objects, which are proportional to the dimensions of the thermal image. Based on this file, the central equipment (i.e., the SAs) was identified using thermography. A ratio of (1.38:1) between the thermal image and the temperature matrix (M_{temp}) was applied to extrapolate the coordinates of the bounding box in order to identify and delimit the temperatures corresponding to the detected region of interest.

Next, a matrix called M_{aux} was generated that contained the temperatures covered by the bounding box area of the main SA, while the remainder of the temperatures were set to zero. However, it was observed that the delimited area included temperatures from the background of the image. To eliminate these, a threshold of 90 % of the ambient temperature was adopted, as it was found that the background typically had temperatures well below this threshold, whereas the region of interest had temperatures higher than this value. Auto-scaling of M_{aux} was performed to allow the remaining temperatures to be treated as pixels of a grayscale image, and a binary matrix M_{bin} was obtained through adaptive thresholding.

A morphological opening process was then applied to Mbin. The structural element used had the shape of an "I," dimensions (5, 50), similar to the SA. This procedure included edge attenuation, fragmentation of narrow connections, and the removal of fine protrusions [33]. A feature extractor was also used to determine the angle of the resulting region (the insulating column of the monitored equipment).

It is noteworthy that the appropriate thresholding and morphological processes were performed using the OpenCV computer vision library in Python. Two specific functions from this library, adaptiveThreshold and morphologyEx, played a fundamental role in this study.

After obtaining the angle of the resulting region, the thermal image and its temperature matrix (M_{temp}) were rotated, and the detection process was reapplied to obtain a more closely fitting bounding box around the main equipment. The previous steps were then repeated.

The reapplication of this process allowed for enhanced segmentation of the SA, and was carried out because some of the thermal images exhibited a slight tilt due to the capture angle. Next, the product of the binary matrix (M_{bin}) and the temperature matrix (M_{temp}) was calculated to obtain the resulting temperature matrix (M_{result}). Finally, the thermal profile was extracted from the central axis of the region of interest in M_{result}.

It is worth noting that the CNN YOLOv5, used for detecting the region of interest, outlines the detected area with bounding boxes aligned either vertically or horizontally. However, if the region to be detected is tilted, the generated bounding box may not fit ideally. As a result, the Intersection over Union (IoU) metric — which represents the ratio between the intersection area and the union area of the predicted and actual bounding boxes — may show lower values compared to situations where the image is correctly aligned vertically or horizontally.

Therefore, the processing of the thermal image, detection using the YOLOv5 CNN, and segmentation through computer vision techniques enabled the extraction of the insulator column's angle. This allowed the rotation of the thermal image to align the insulator column vertically, resulting in a bounding box that more accurately fits the main equipment and improved segmentation of the insulator column. Additionally, after rotating the thermal image, it was possible to extract a vertically aligned thermal profile that follows the central axis of the equipment along its entire length.

Fig. 3 shows an example of the processing of a thermal image, before and after rotation.

2.4. Alignment of thermal profiles using dynamic time warping

Due to subtle differences in the profile length, phase shifts, and amplitude differences among the thermal profiles, we carried out interpolation, normalization, and data alignment procedures. Fig. 4 shows a flowchart illustrating the process of aligning the thermal profiles.

Interpolation based on the spline technique was performed to adjust length mismatch among the extracted thermal profiles, which occurred due to the number of pixels in the thermal image corresponding to the area of interest. This quantity is influenced by the capture angle and distance, resulting in profiles of varying lengths. Interpolation was applied to fill in the empty spaces or to extend the profiles to ensure consistency for a comparative analysis.

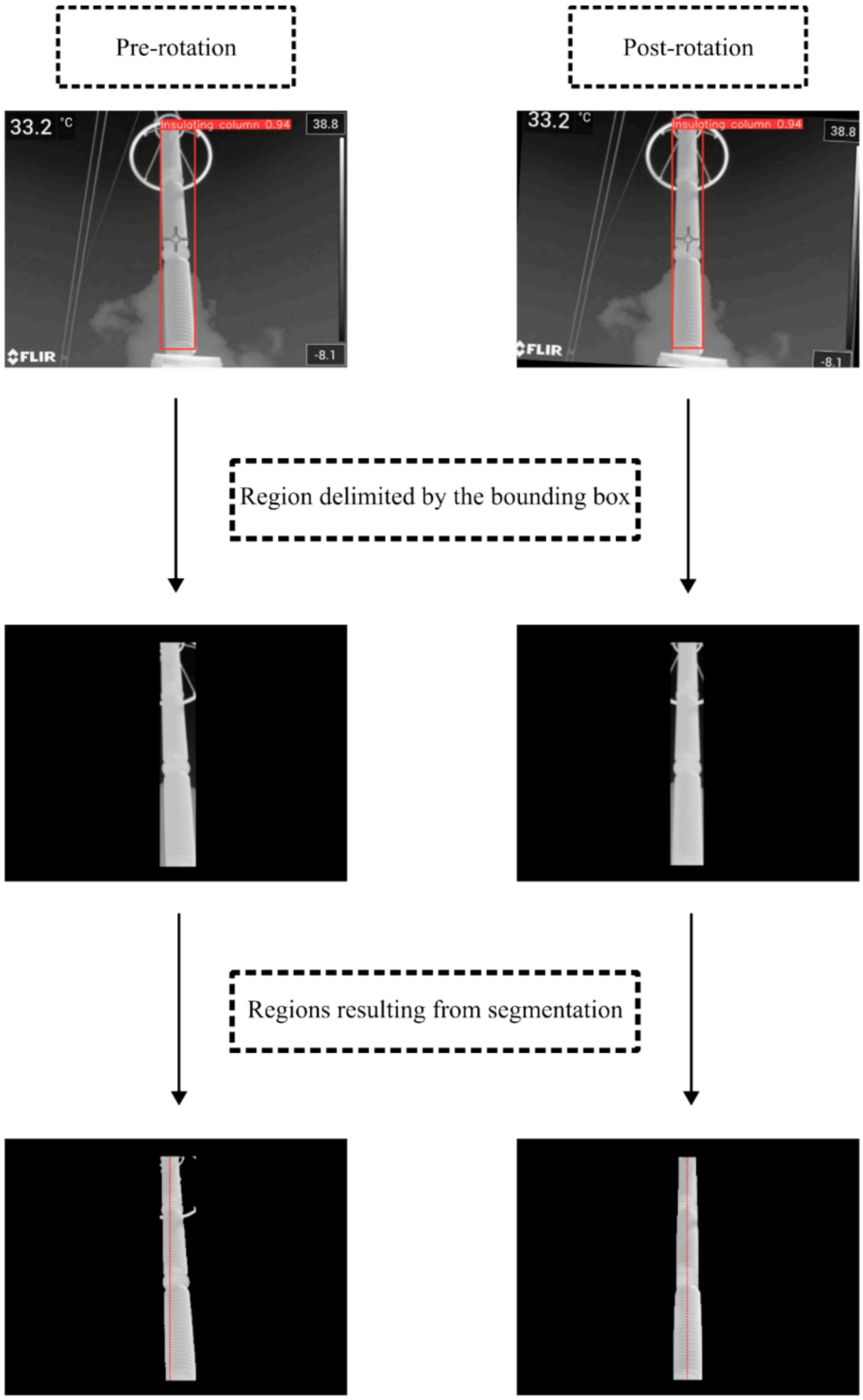

Fig. 3. Processing of a thermal image, before and after rotation.

Next, normalization was applied, which involved removing the mean value and adjusting the signal values so that the mean became zero. This facilitated the alignment and comparison of the thermal profiles by eliminating differences in amplitude.

The aim of the alignment process was to correct any horizontal phase differences between the thermal profiles of the equipment and the reference profile. This process synchronized the profiles to ensure an accurate comparison between them, and was performed using a Python implementation of DTW (described in Section 2.5). After alignment, to enable us to evaluate the temperatures based on their absolute values, the respective mean values of each profile were added.

When aligning the signals (analyzed and reference), the DTW algorithm was used with an adaptive Sakoe-Chiba constraint bandwidth [34,35]. This window width determines a tolerance range that allows horizontal shifts in the search for the ideal match between the signals. In this study, the window width was established based on the average distances between peaks in the signals, and was set to a value equal to twice the largest of these distances. This approach was developed empirically by analyzing the thermal profiles and applying various window widths. The metric used was the Euclidean distance. The

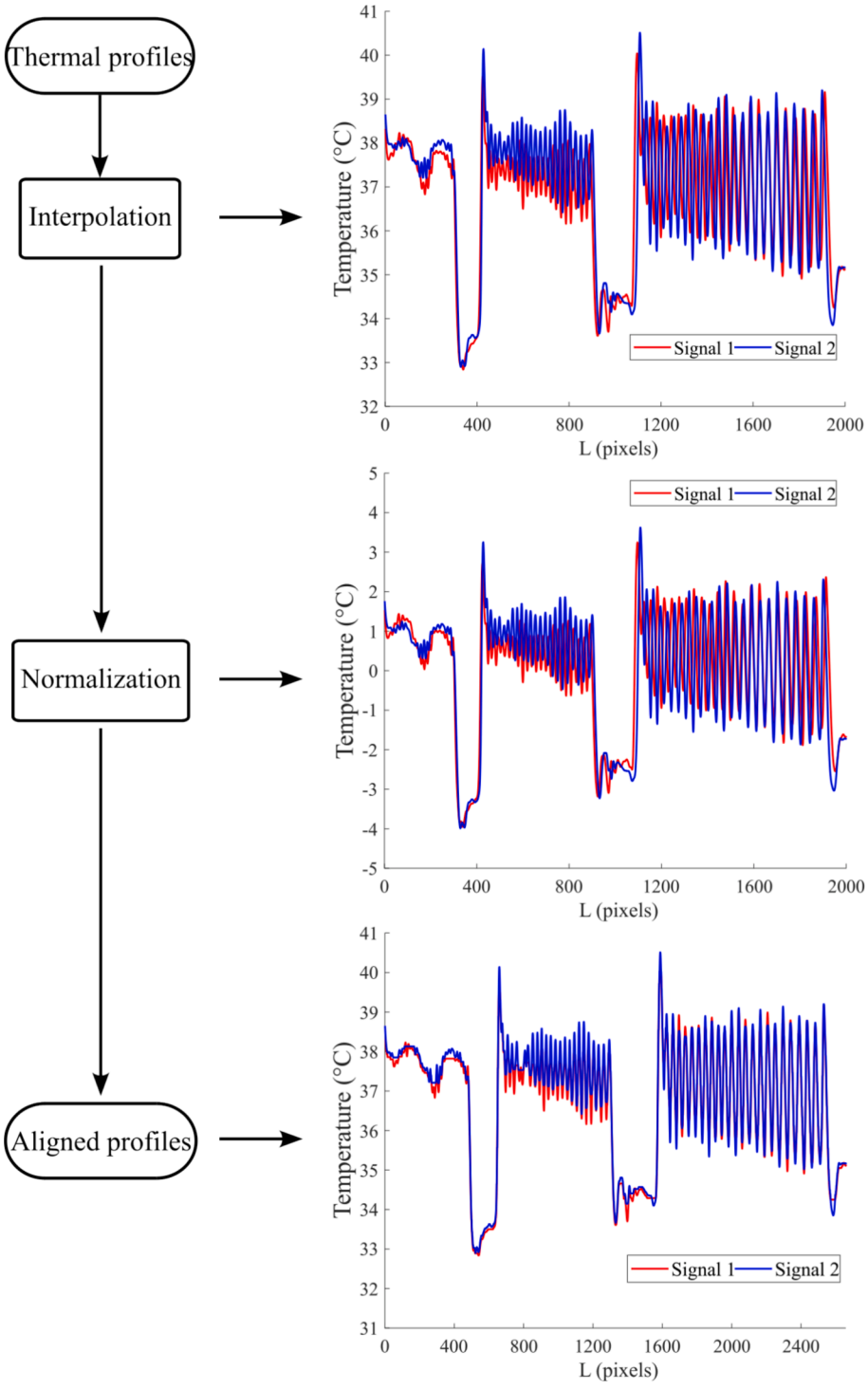

Fig. 4. Alignment process of thermal profiles.

implementation of this method resulted in a reduced computational cost and enhanced accuracy of comparison, and enabled the algorithm to adapt to temporal variations. Furthermore, this range constraint prevented inappropriate alignments and provided greater control over the algorithm's sensitivity, making it more efficient and accurate when comparing temporal sequences with different lengths or shifts.

In this process, variations in the number of pixels and temperature extracted were addressed through interpolation, normalization, and alignment, thus ensuring a more precise and reliable comparison of thermal profiles for equipment analysis and diagnosis. When performing the alignment process between thermal profiles, the total cost (c_p) representing the distance between the signals was determined, in order to provide a more detailed assessment of the similarity between thermal profiles and make the analysis process even more robust and reliable.

Given the above, proper alignment between thermal profiles was essential for enhancing the effectiveness in defect detection and equipment diagnosis. If the alignment is not performed correctly, the likelihood of generating false positives or false negatives increases significantly due to the comparison of non-matching points. Therefore, the entire described procedure was adopted to maximize alignment

efficiency and minimize the occurrence of false positives and false negatives.

Thus, it was possible to compare corresponding points between the two signals to calculate the percentage variation between the temperatures of the analyzed signal and the reference signal after alignment. This allows for a more detailed analysis of ZnO surge arresters, facilitating the identification and anticipation of thermal anomalies in different regions. As a result, more accurate information about the integrity of electrical equipment was obtained, enabling the early identification of potential issues, determining their effect (heating or cooling), and approximating their location.

2.5. Equipment diagnosis

To diagnose the integrity of ZnO SAs, we modified the equation presented by Chou et al. [18], which was originally applied to points rather than signals. This resulted in Eqs. (1) and (2):

$$\Delta T_{threshold}(i) = \frac{\Delta T_{signals}(i)}{signal_{reference}(i)} 100\%, \quad (1)$$

$$\Delta T_{signals}(i) = signal_{analyzed}(i) - signal_{reference}(i) \quad (2)$$

where $i \in [1 : N]$, and $N \in \mathbb{N}$; $signal_{analyzed}$ is the analyzed thermal profile; $signal_{reference}$ is the reference thermal profile; $\Delta T_{signals}$ is the point-by-point variation between the monitored and reference signals, $\Delta T_{threshold}$ is the percentage variation between the analyzed profile and the reference profile.

In this way, the percentage variation between the temperatures of the analyzed signal and the reference signal was calculated after alignment. This allowed for a more detailed analysis of the ZnO SA, and enabled the identification and/or anticipation of thermal anomalies in different regions. It was therefore possible to obtain more accurate information about the integrity of the electrical equipment, identify potential issues at early stages, and to determine their effects (heating or cooling) and their approximate locations.

Finally, the qualitative rules presented in Table 1 for the analysis of electrical equipment were defined. These rules were based on those of Chou and Yao [18], and were applied to classify the different operational conditions of high-voltage electrical equipment through the proposed thermal inspection methodology.

It is worth noting that the thresholds used in this study were derived from the research conducted by [18]. According to this research, the threshold values correspond to those applied in practice and were determined based on successive thermographic inspections of defective equipment in operation.

It is noteworthy that the proposed method uses a CNN to enhance the segmentation process, ensuring a more accurate extraction of the thermal profile. This allows the automatic extraction of the thermal profile from a thermal image. After processing the image and extracting the thermal profile, it is aligned with a reference profile, allowing an accurate point-by-point comparison between the two. Finally, a point-by-point percentage variation assessment between the thermal profiles is conducted to identify any variations that may indicate an abnormal operating condition.

Therefore, if a monitored piece of equipment exhibits $\Delta T_{threshold}$ values outside the limits defined as normal, it will be classified as having a thermal anomaly. Depending on the severity of this anomaly, the equipment may be classified under “emergency” or “critical” conditions.

Table 1
Qualification classes.

Condition	Negative percentage variation ($\Delta T_{threshold}$)	Positive percentage variation ($\Delta T_{threshold}$)
Normal	$-9 \leq \Delta T_{threshold}(i) < 0\%$	$0\% \leq \Delta T_{threshold}(i) \leq 9\%$
Emergency	$-90\% \leq \Delta T_{threshold}(i) < -9\%$	$9\% < \Delta T_{threshold}(i) \leq 9\,0\,\%$
Critical	$\Delta T_{threshold}(i) < -90\%$	$90\,\% < \Delta T_{threshold}(i)$

3. Results and discussion

In this section, we present the results obtained from the methodology described above. We first evaluate the performance of the algorithm for detecting the insulating column of the SA. Table 2 presents the main performance results of the detection algorithm.

From Table 2, it can be observed that the detection algorithm achieved precision and recall scores of 0.861 and 0.855, respectively, indicating that the model had a strong capability to detect and correctly identify the equipment of interest. The other indices were also good, with mAP50 reaching a value of 0.903. This shows that the model has a high object detection rate with a prediction confidence of 50 % or higher.

However, the mAP50:95 had a value of 0.615, indicating that the model’s performance slightly decreases when a broader confidence range from 50 % to 95 % is considered, although this decrease did not result in significant detriment to the diagnostic method, thus demonstrating that the model was capable of making reliable detections even at lower confidence levels.

We also analyzed the robustness of the thermal camera with respect to subtle changes in angle and distance in sequential thermographic images, taking into account environmental effects. For this purpose, thermal images of the same equipment were captured in successive moments, showing that although they were taken from similar angles and distances, the extracted thermal profiles exhibited slight discrepancies. Figs. 5 and 6 show eight thermographic images of the same SA and their respective thermal profiles from the central axis. This highlights the need to apply a signal alignment process to ensure an accurate comparison between the points of the evaluated thermal profiles.

From Fig. 6 it is evident that there is a phase shift between the thermal profiles; this hinders the application of the point-to-point diagnostic method, since there is misalignment between the peaks and valleys, leading to a comparison between the temperatures of non-corresponding regions. To address this issue, the profiles were aligned using DTW, followed by the application of Eqs. (1) and (2).

In this analysis, the reference signal was taken as the thermal profile of signal 1, corresponding to the thermographic image in Fig. 5(a), and the others were considered to be the analyzed signals. Fig. 7 shows signals 1 and 2 (for the reference and analyzed images, respectively) after alignment.

From Fig. 7, it is evident that the peaks and valleys have been aligned, meaning that we can use Equations (3) and (4) to perform an evaluation of the temperatures at corresponding points. Fig. 8 shows the values of $\Delta T_{\text{threshold}}$ between signal 1 (reference) and signal 2 (analyzed).

From Fig. 8, it can be seen that the maximum and minimum values of $\Delta T_{\text{threshold}}$ were 1.13 % and −1.0 %, respectively. From an analysis of the other signals (3 to 8) with signal 1 as the reference, it was found that the maximum and minimum values of $\Delta T_{\text{threshold}}$ were 4.16 % and −1.60 %, respectively. These results demonstrate that when the proposed method was applied, the values of the percentage variations remained between 9 % and 9 %, as indicated in Table 1, which is within the normal range. The distance values between the signals ranged from 152.05 to 287.49.

It is important to emphasize that the diagnostic process was not compromised despite the intrinsic measurement error of the thermal imager, variations in distance and angle, and the influence of environmental factors (radiation, shading, wind direction, etc.), which resulted in variations in both positive and negative $\Delta T_{\text{threshold}}$ values. To some

Table 2
Performance metrics for the detection algorithm.

Precision (ρ)	*Recall* (*r*)	*mAP*50	*mAP*50 : 95
0.861	0.855	0.903	0.615

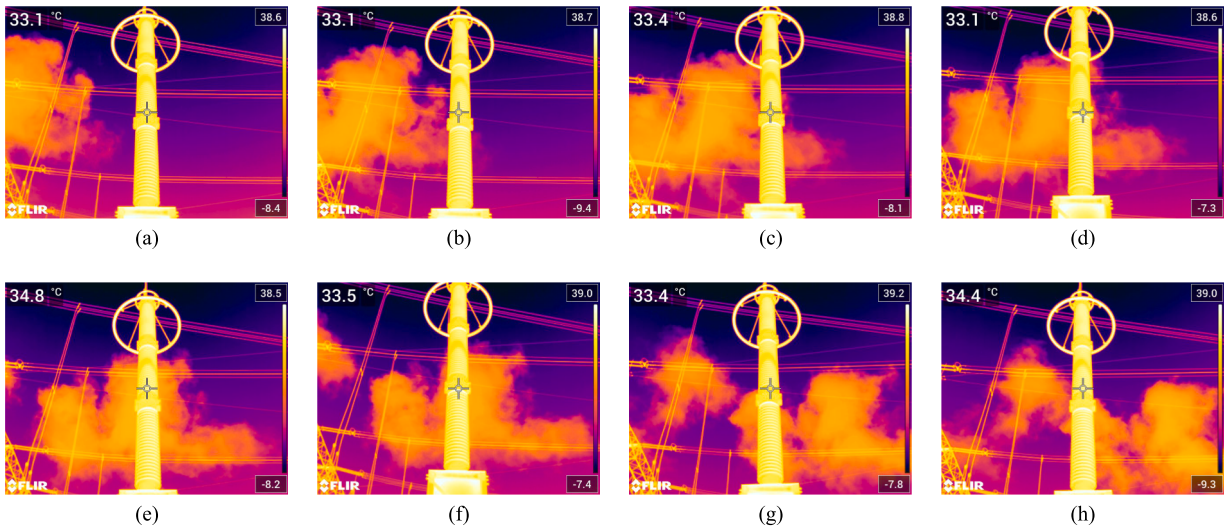

Fig. 5. (a) Thermography 1; (b) Thermography 2; (c) Thermography 3; (d) Thermography 4; (e) Thermography 5; (f) Thermography 6; (g) Thermography 7; (h) Thermography 8.

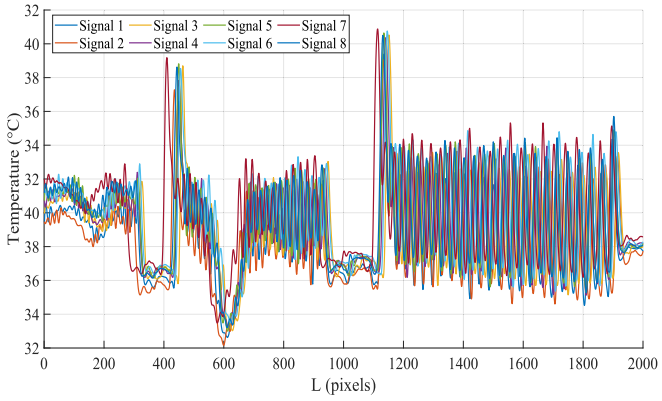

Fig. 6. Thermal profiles from eight thermographs of the same surge arrester.

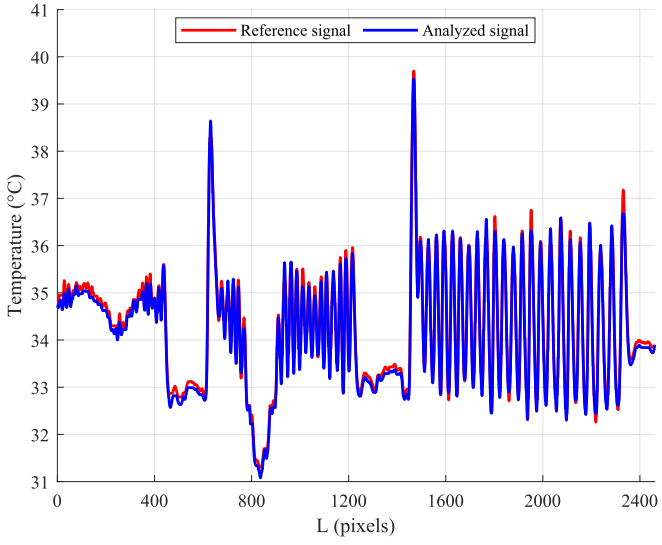

Fig. 7. Signals 1 and 2 (reference and analyzed signals) after alignment.

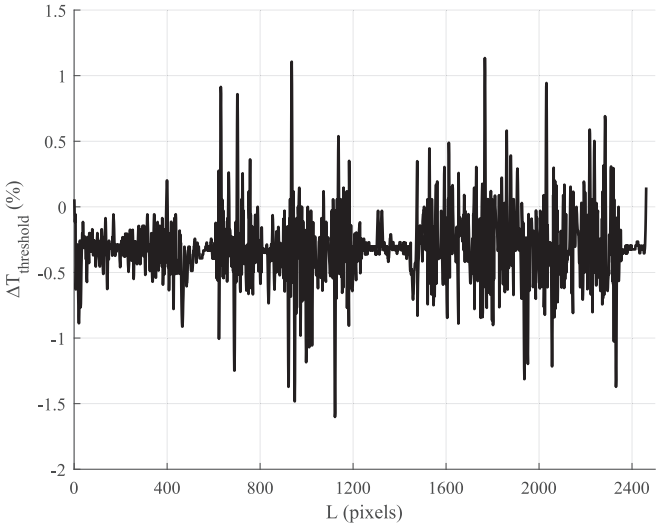

Fig. 8. $\Delta T_{threshold}$ between signals 1 and 2 (reference and analyzed signals, respectively).

extent, this demonstrates the robustness and effectiveness of the proposed method.

In the analysis of the different phases of the SAs, the thermal profiles of phase A were used as reference signals, while the analyzed profiles were those of the other phases (B and C), which were collected at the same time and at similar angles. After aligning the profiles, the values of $\Delta T_{threshold}$ and the distance between signals were determined for the six time slots (10 am to 11 am and 4 pm to 7 pm). Table 3 presents the values of $\Delta T_{threshold}$ and maximum distance for each case.

From Table 3, it can be seen that the $\Delta T_{threshold}$ values were within a range considered normal (−9% to 9 %). The differences in the $\Delta T_{threshold}$ values for each time period can be attributed to various factors, such as the different shaded areas and temperature variations in the SA junctions. The junctions were composed of metallic materials, which made them more susceptible to the influences of solar radiation and ambient temperature. These differences in shaded areas and temperature among the equipment's connections led to heterogeneous temperature distributions.

The thermal profiles extracted during the morning period were more strongly influenced by solar radiation, resulting in shaded areas and

Table 3
$\Delta T_{threshold}$ for each angle in the five time slots analysed.

Reference phases	Analyzed phases	Time	$\Delta T_{threshold\ Minimum}$	$\Delta T_{threshold\ Maximum}$	Maximum distance
A	B and C	10 h	−1.99	6.11	344
		11 h	−5.95	6.7	313.44
		16 h	−0.58	5.87	350.83
		17 h	−0.60	4.05	263.05
		18 h	−0.72	2.51	86.32
		19 h	−1.36	1.71	92.29

temperature differences in the SA connections. From Table 3, it becomes apparent that values corresponding to this morning period (10 am to 11 am) show the largest variations between the maximum and minimum $\Delta T_{threshold}$ values. This pattern can also be observed in the values for the 4 pm period, during which there is still considerable solar radiation. Fig. 9 shows the aligned thermal profiles and $\Delta T_{threshold}$ values from the thermal images of the SA (phases A and C) at 11 am.

It is evident from the aligned signals that there are thermal discrepancies in the SA connections (points 600 and 1400). In these regions, which exhibit thermal heterogeneity, the $\Delta T_{threshold}$ curve reaches its highest peak and lowest valley. Hence, the influence of the environment on the temperature of the equipment can result in points of thermal discrepancy, and consequently false positives. However, the proposed method demonstrates robustness to the influence of the environment, enabling a clear perception of the main points affected by solar radiation and their locations, and allowing for a more precise analysis.

In contrast, the thermographic images captured in the late afternoon and the beginning of the evening (6 pm–7 pm) show the smallest thermal discrepancies, and significant thermal discrepancies due to environmental influence are not noticeable. Fig. 10 shows aligned thermal profiles and $\Delta T_{threshold}$ for SA thermographic images (phase A and C) taken at 7 pm.

An analysis of the aligned signals shows that they are similar, with no significant thermal discrepancies. This observation is also reflected in the values of the $\Delta T_{threshold}$ curve, which had small variations.

Finally, in order to validate the proposed methodology and the classification method, thermal images of a healthy SA and an SA with intentionally introduced defects from [3] were considered. Fig. 11 shows the thermal profiles extracted from a healthy SA and one with sealing loss.

From Fig. 11, it can be observed that although the loss of sealing caused a cooling effect on the equipment, it did not lead to significant deformations in the thermal profile. These two characteristics of this case make it difficult to detect or classify the defect. The intentionally poor sealing resulted in a gas exchange with the outside and air circulation within the SA. This led to faster heat dissipation from the varistors, especially in the lower region.

Fig. 12 shows thermographic images of the SA in a healthy condition and after the loss of sealing, the aligned thermal profiles after applying DTW, and the $\Delta T_{threshold}$ curve, representing the percentage temperature difference between the healthy reference signal and the analyzed signal (with a loss of sealing).

From Fig. 12, it is evident that after applying the thermal profile alignment technique using DTW, the peaks and valleys of the profiles were correctly aligned, thus enabling a comparison and the diagnostic process. Furthermore, it is noticeable that the $\Delta T_{threshold}$ values are negative, indicating cooling of the equipment due to the defect. An analysis of the $\Delta T_{threshold}$ curve reveals that several points have values below the −9 % threshold, with the lowest recorded value being −11.65 %. The most critical point is located near point 2400 (bottom of the equipment), as this region is the most affected by the defect.

It is important to emphasize that although DTW causes deformations in the signal in order to align corresponding points and minimize the Euclidean distance, these deformations (such as the plateau near the points around 2400 in Fig. 12) do not lead to erroneous analyses of the fault locations. In other words, despite the changes induced by DTW, identification of the areas affected by the defect remained accurate and reliable.

The proposed method therefore enabled identification of the defect and the associated thermal anomaly (in this case, cooling), while also providing precise information about the location of the fault in the equipment. Table 4 presents the $\Delta T_{threshold}$ values corresponding to each type of defect and case, as well as the distance between the signals determined by the Euclidean method.

From Table 4 it can be seen that the proposed method correctly classified the condition of the equipment in all 12 cases, resulting in an

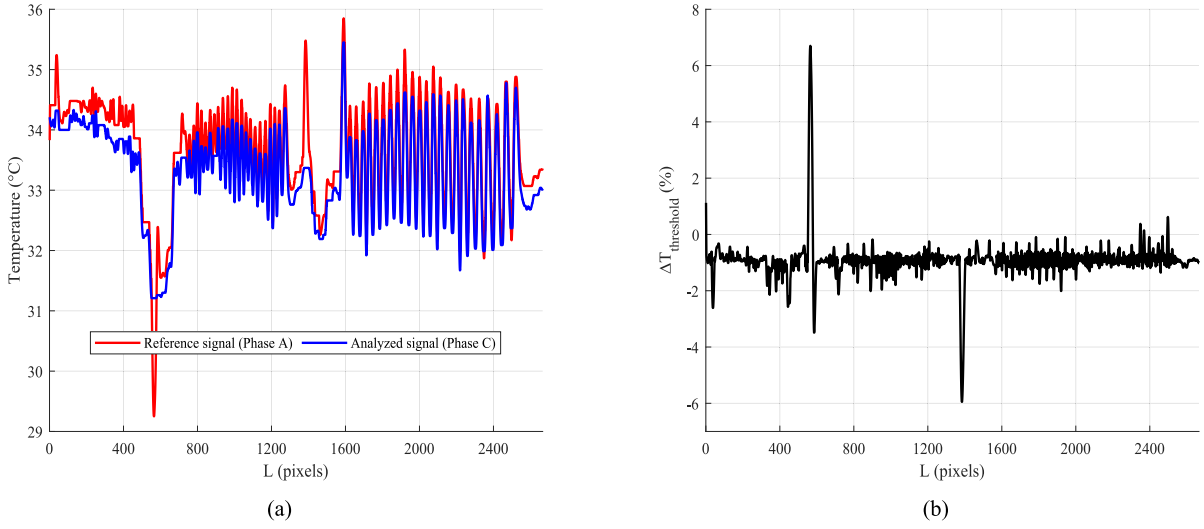

Fig. 9. (a) Thermal profiles from thermal images of a surge arrester (phases A and C) at 11 am; (b) $\Delta T_{threshold}$ from thermal images of surge arresters (phases A and C) at 11 am.

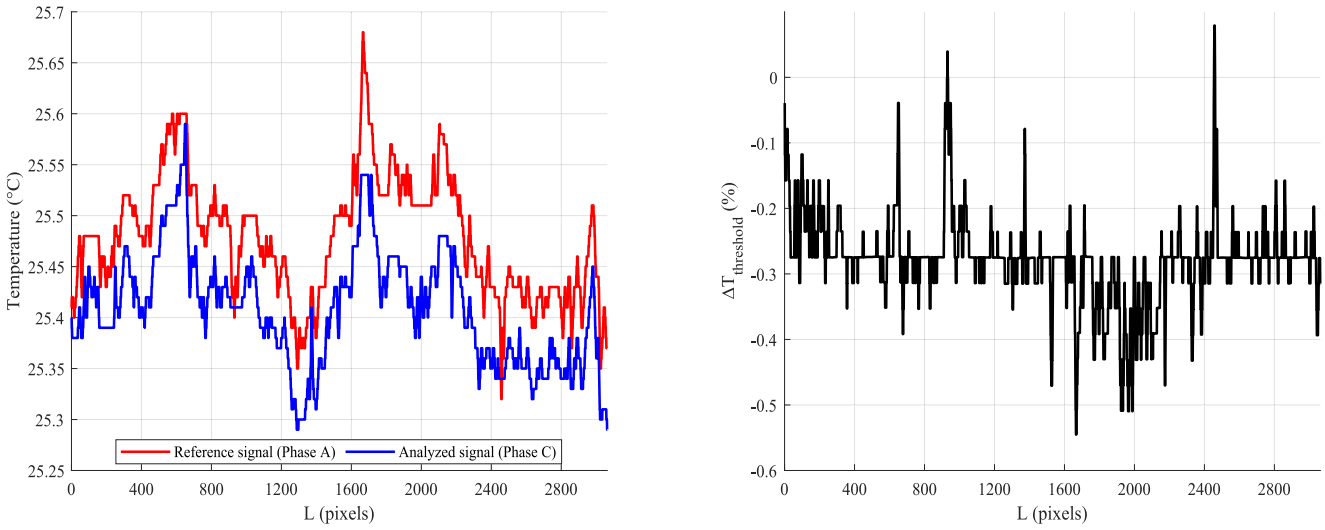

Fig. 10. (a) Thermal profiles of surge arrester thermographs (phases A and C) taken at 7 pm; (b) $\Delta T_{threshold}$ for surge arrester thermographs (phases A and C) taken at 7 pm.

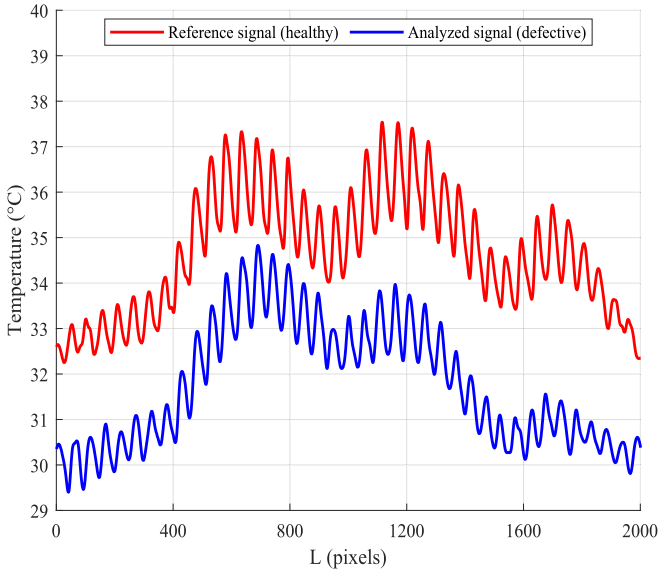

Fig. 11. Thermal profiles extracted from a healthy surge arrester (reference signal) and one with loss of sealing (analyzed signal).

accuracy rate of 100 %. In cases where $\Delta T_{threshold}$ had negative values of below −9 %, this indicated that the defect caused cooling at specific points in the equipment, whereas positive values above 9 % indicated that the defect caused heating points in the equipment. Although 12 cases are illustrated, considering the full dataset of 409 images, the proposed method maintained the same accuracy rate.

Regarding the defects that caused a thermal reduction, in short-circuit cases, a redistribution of voltage along the column and a decrease in heating due to the Joule effect in the affected region were observed. This behavior was expected, as the short-circuited varistor does not exhibit significant heating, resulting in a redistribution of voltage to the other varistors [3].

In the case of a loss of sealing, the thermal reduction may have occurred due to the circulation and exchange of gases inside the surge arrester. This phenomenon accelerated heat dissipation by the varistors, especially in the lower region of the equipment [3].

Finally, in the case of insulating column misalignment, a possible explanation for the thermal reduction could be the redistribution of voltage or the formation of preferential conduction channels in the contact areas of the misaligned varistors [3].

From Fig. 12, representing a loss of airtightness (case 2), we see that the reference signals and the analyzed (faulty) signal show similar trends, with the discrepancy occurring only in the final third of the curve.

Furthermore, an analysis of the distance between the signals indicates that in most of the cases with imposed defects, the signal distances were on the order of 1,000. In contrast, for a short-circuit across a set of varistors, a short-circuit across a subsequent set of varistors, and the second case of a loss of airtightness, the signal distances were on the order of hundreds, with a magnitude similar to the distance between healthy signals, as presented in Tables 3 and 4.

These results demonstrate the potential of the proposed method, and highlights that the distance between signals, as a measure of similarity, may be an initial indicator of a defect. In cases where the signals are close, meaning they have a high level of similarity but there is a defect, the $\Delta T_{threshold}$ curve is proven to be crucial for an accurate diagnosis of the equipment.

Finally, it is worth noting that signals with a high distance (meaning low similarity) are more challenging to align using DTW. A significant dissimilarity between signals can result in less precise alignment, and may require more computational resources. However, despite this effect, the $\Delta T_{threshold}$ curve numerically points the presence of a defect. Hence, in cases where signal alignment is less precise due to a significant dissimilarity between the reference and analyzed signals, the distance parameter can confirm this dissimilarity and may indicate a potential defect. A combination of $\Delta T_{threshold}$ and the degree of similarity between signals, measured by the distance value, proves to be an important metric in the thermal analysis of electrical equipment, especially SAs.

4. Conclusion

This study has presented a method for diagnosing thermal anomalies in ZnO SAs. The method used here, based on thermal images and temperature matrix processing, provides uniform detection and segmentation, resulting in consistent thermal profiles. This ensures the accurate identification of thermal anomalies in SAs without unwanted interference from other components.

It is important to emphasize that despite the inevitable variations

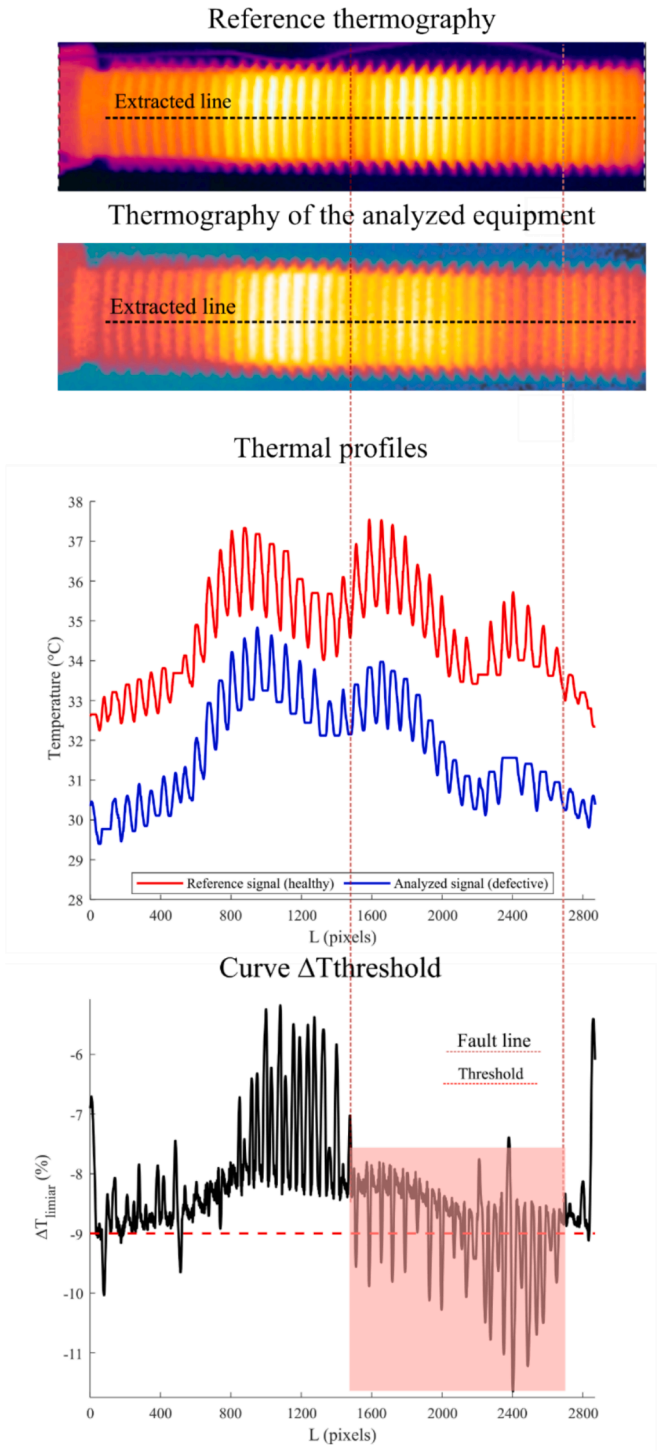

Fig. 12. Thermographic images of the SA in a healthy condition and after the loss of sealing; aligned thermal profiles; $\Delta T_{\text{threshold}}$ curve.

arising from the measurement error of the thermal camera, fluctuations in distance and angle, and environmental influences, the results were not compromised. In the case analyzed here, it was observed that the maximum $\Delta T_{threshold}$ values varied from −1.60 % to 4.16 %, but these variations did not hinder the proper alignment and accurate evaluation of the results.

In a further analysis, it was found that the temperatures of objects other than the insulating column, such as the SA's support pedestal and its connections, were included in all profiles without negatively affecting the diagnosis (Table 3), with $\Delta T_{threshold}$ values ranging from −5.95 % to 6.11 %.

Table 4
$\Delta T_{\text{threshold}}$ of the thermal profiles extracted from each defect and analyzed cases.

Defect	Case	$\Delta T_{\text{threshold Minimum}}$	$\Delta T_{\text{threshold Maximum}}$	Distance
Short circuit inside a single varistor	1	−22.47 %	−11.38 %	1250
Short circuit on a set of varistors	2	−24.96 %	−19.56 %	514.88
Short circuit on separate varistors	3	−47.29 %	−23.57 %	6928.5
Short circuit on subsequent varistor sets	4	−14.82 %	−6.59 %	710.84
Broken varistor	5	−28.46 %	−11.91 %	2552.7
Loss of airtightness	6	−47.13 %	−22.23 %	7208
	7	−11.64 %	−5.18 %	570.98
Internal humidity	8	2.53 %	49.97 %	4325
	9	−7.57 %	27.83 %	2739.4
Active column misalignment	10	−47.77 %	−19.99 %	7345.2
Surface pollution	11	−14.52 %	24.38 %	6292.2
	12	−15.04 %	42.97 %	8405.5

In the final analysis, the proposed method was applied to both a healthy SA and SAs with induced defects, and achieved a 100 % accuracy rate. The algorithm could also identify whether the defect resulted in cooling or heating of the equipment. Furthermore, if any of the defects were likely to evolve, our technique could detect this and trigger alerts for the operators of these devices. This demonstrates the effectiveness of our method in terms of identifying thermal anomalies and their locations, and providing valuable information about the condition of the surge arresters.

Additionally, when comparing the proposed method with the study presented in [3], which used a neural network to classify the presence of defects and employed a manual process for thermal profile extraction, it was observed that the study achieved an accuracy rate of 99.4 % in defect classification. Therefore, the proposed method not only improved accuracy rates but also automated the thermal profile extraction process.

The distance between the reference and analyzed signals was also found to be an initial indicator of a potential defect. If the signals are not well aligned due to significant dissimilarity, the distance parameter can confirm this dissimilarity and indicate a potential defect.

The proposed method provides a reliable approach for diagnosing faults in SAs, and has the potential to be applied to any other type of high-voltage equipment where faults manifest through thermal anomalies. This can enhance preventive maintenance and increase the operational safety of these devices. Moreover, the method can precisely identify, localize, and analyze thermal anomalies, including under real operating conditions, despite the presence of variations and interference.

Moreover, it is possible to explore other detection methods that allow for a more precise delineation of the area of interest in the equipment. This can be achieved through the use of advanced segmentation algorithms or more sophisticated image processing techniques, such as Mask R-CNN and U-Net. Additionally, it is advisable to compare different CNN architectures to evaluate which one offers the best performance in segmentation and, consequently, in enhancing the extraction of the thermal profile, with the aim of improving the diagnostic process of the monitored equipment.

Finally, additional techniques for signal alignment could be explored, as well as optimization of windowing and DTW constraints. These approaches could potentially improve the alignment process and enhance the robustness of the method presented in this article. Adopting more advanced methods may lead to greater accuracy and efficiency in signal analysis, thereby strengthening diagnostic effectiveness. Furthermore, one could explore, for example, the equations and thresholds presented in [17], or propose new equations and thresholds

with the aim of enhancing and extending the work presented.

CRediT authorship contribution statement

Bruno Vinicius Silveira Araujo: Writing – review & editing, Writing – original draft, Visualization, Validation, Software, Methodology, Investigation, Formal analysis, Data curation, Conceptualization. **Gustavo Aragão Rodrigues:** Writing – review & editing, Validation, Methodology, Investigation, Formal analysis, Conceptualization. **Johnny Herbert Paixão de Oliveira:** Writing – review & editing, Visualization, Software, Data curation. **George Victor Rocha Xavier:** Writing – review & editing, Supervision, Project administration, Methodology, Investigation, Data curation, Conceptualization. **Ulisses Daniel Enes de Souza Lebre:** Writing – review & editing, Supervision, Resources, Project administration, Conceptualization. **Charles Antony Cordeiro de Araujo:** Writing – review & editing, Resources, Project administration, Investigation, Conceptualization. **Eduardo Oliveira Freire:** Writing – review & editing, Writing – original draft, Supervision, Methodology, Investigation, Formal analysis, Data curation, Conceptualization. **Estácio Tavares Wanderley Neto:** Writing – review & editing, Resources, Data curation. **Tarso Vilela Ferreira:** Writing – review & editing, Visualization, Validation, Supervision, Resources, Project administration, Funding acquisition, Data curation, Conceptualization.

Declaration of competing interest

The authors declare that they have no known competing financial interests or personal relationships that could have appeared to influence the work reported in this paper.

Acknowledgment

This work was developed as part of the project GImpSI - Gestão dos Impactos da Salinidade em Isolamentos with INESC P&D Brasil and ENEVA S.A., under the framework of the R&D Program of the Brazilian Electricity Regulatory Agency, code PD-11278-0001-2021. This work was supported in part by the Coordination for the Improvement of Higher-Level Personnel (CAPES) –Finance Code 001.

Data availability

Data will be made available on request.

References

[1] J.J. Grainger, W.D. Stevenson Jr, Power system analysis. McGraw-Hill Series in Electrical and Computer Engineering, 1994.
[2] V. Hinrichsen, Metal-Oxide Surge Arresters in High-Voltage Power Systems. Fundamentals, Siemens AG, Erlangen, Germany, 2012.
[3] E.T. Wanderley Neto, E.G. da Costa, M.J.A. Maia, Artificial Neural Networks Used for ZnO Arresters Diagnosis, IEEE Trans. Power Delivery 24 (3) (2009) 1390–1395, https://doi.org/10.1109/TPWRD.2009.2013402.
[4] S. Bagavathiappan, et al., Infrared thermography for condition monitoring – A review, Infrared Phys. Technol. 60 (2013) 35–55.
[5] Y. Lin, et al., Automatic display temperature range adjustment for electrical equipment infrared thermal images, Energy Procedia 141 (2017) 454–459.
[6] H. He, et al., Insulator infrared image denoising method based on wavelet generic Gaussian distribution and MAP estimation, IEEE Trans. Ind. Appl. 53 (4) (2017) 3279–3284.
[7] B.S. Li, et al., Infrared Image Denoising Based on Peer Groups with Median Filtering and Wiener Filtering, Appl. Mech. Mater. (2013) 1059–1062.
[8] C. Shanmugam, E.C. Sekaran, IRT image segmentation and enhancement using FCM-MALO approach, Infrared Phys. Technol. 97 (2019) 187–196.
[9] S. Gao, et al., in: Infrared Thermal Image Fault Detection Based on YOLOV3-L, IEEE, 2022, pp. 175–178.
[10] X. Li, in: Design of Infrared Anomaly Detection for Power Equipment Based on YOLOv3, IEEE, 2019, pp. 2291–2294.
[11] Z. Zhao, et al., Aggregating deep convolutional feature maps for insulator detection in infrared images, IEEE Access 5 (2017) 21831–21839.
[12] T. Zhao, et al., in: Thermal Image Skeleton Extraction and Intelligent Recognition of Power Equipment, IEEE, 2020, pp. 4331–4335.
[13] H. Zheng, et al., An infrared image detection method of substation equipment combining iresgroup structure and centernet, IEEE Trans. Power Delivery 37 (6) (2022) 4757–4765.
[14] J.S. Kim, K.N. Choi, S.W. Kang, Infrared thermal image-based sustainable fault detection for electrical facilities, Sustainability 13 (2) (2021) 557.
[15] R.O.A. Takeuchi, et al., Comparison of Traditional Image Segmentation Methods Applied to Thermograms of Power Substation Equipment, Energies 15 (20) (2022) 7477.
[16] A. Jiang, et al., in: Research on Infrared Image Recognition Method of Power Equipment Based on Deep Learning, IEEE, 2020, pp. 1–4.
[17] Y. Cao, X. Gu, Q. Jin, in: Infrared Technology in the Fault Diagnosis of Substation Equipment, IEEE, 2008, pp. 1–6.
[18] Chou, Y. C., & Yao, L. (2009). Automatic diagnostic system of electrical equipment using infrared thermography. In 2009 international conference of soft computing and pattern recognition (pp. 155-160). IEEE.
[19] Zhang, D., et al. (2021). Error Analysis of Relative Temperature Difference Discrimination Method for Infrared Temperature Measurement of Low Temperature Electrical Equipment. In 2021 IEEE 3rd Eurasia Conference on IOT, Communication and Engineering (ECICE) (pp. 514-517). IEEE.
[20] T. Li, et al., Temperature distribution characteristics and heat defect judgment method based on temperature gradient of suspended composite insulator in operation, IET Gener. Transm. Distrib. 15 (18) (2021) 2554–2566.
[21] I. Ullah, et al., Deep learning image-based defect detection in high voltage electrical equipment, Energies 13 (2) (2020) 392.
[22] K. Wang, et al., Thermal Defect Detection for Substation Equipment Based on Infrared Image Using Convolutional Neural Network, Electronics 10 (16) (2021) 1986.
[23] L. Su, et al., Infrared-Visual Image Fusion and CNN Model in Electrical Faults Diagnosis, J. Phys. Conf. Ser. 042068 (2021).
[24] M. Lu, H. Liu, X. Yuan, Thermal Fault Diagnosis of Electrical Equipment in Substations Based on Image Fusion, Traitement Du Signal 38 (4) (2021).
[25] Y. Wang, Y. Yin, J. Ren, Research on thermal state diagnosis of substation equipment based on infrared image, Adv. Mech. Eng. 11 (4) (2019) 1687814019828551.
[26] B. Wang, et al., Automatic fault diagnosis of infrared insulator images based on image instance segmentation and temperature analysis, IEEE Trans. Instrum. Meas. 69 (8) (2020) 5345–5355.
[27] S. Han, et al., A smart thermography camera and application in the diagnosis of electrical equipment, IEEE Trans. Instrum. Meas. 70 (2021) 1–8.
[28] H. Zheng, et al., Intelligent Diagnosis Method of Power Equipment Faults Based on Single-Stage Infrared Image Target Detection, IEEJ Trans. Electr. Electron. Eng. 17 (12) (2022) 1706–1716.
[29] J. Wang, et al., Online monitoring of electrical equipment condition based on infrared image temperature data visualization, IEEJ Trans. Electr. Electron. Eng. 17 (4) (2022) 583–591.
[30] FLIR. User's manualFLIRT8xxseries. FLIR Systems. [S.l.]. 2019.
[31] J. Redmon, et al., You only look once: Unified, real-time object detection, in: Proceedings of the IEEE Conference on Computer Vision and Pattern Recognition, 2016, pp. 779–788.
[32] Redmon, J., & Farhadi, A. (2016). You Only Look Twice: Multi-Scale Object Detection in Satellite Imagery with Convolutional Neural Networks. Medium. Retrieved from https://medium.com/the-downlinq/you-only-look-twice-multi-scale-object-detection-in-satellite-imagery-with-convolutional-neural-38dad1cf7571.
[33] R.C. Gonzalez, R.E. Woods 3rd, Digital Image Processing, Prentice Hall, 2008.
[34] Senin, P. (2008). Dynamic time warping algorithm review. Information and Computer Science Department University of Hawaii at Manoa Honolulu, USA, 855, p. 1-23.
[35] Z. Geler, et al., Dynamic Time Warping: Itakura vs Sakoe-Chiba, in: IEEE International Symposium on INnovations in Intelligent SysTems and Applications (INISTA), 2019, pp. 1–6.